Electronic Supplementary Material (ESI) for Journal of Materials Chemistry A.

## Electronic Supplementary Information

# Robust electrografted interfaces on metal oxides for electrocatalysis - an *in situ* spectroelectrochemical study

Tomos G.A.A Harris[1,2], Robert Götz[1,3], Pierre Wrozlek[4], Victoria Davis[2], Caroline E. Knapp[5], Khoa Ly[6], Peter Hildebrandt[1], Matthias Schwalbe[4], Inez Weidinger[3], Ingo Zebger[1]*, Anna Fischer[2]*

*[1] Technische Universität Berlin, Institut für Chemie, PC 14, Str. des 17. Juni 135, 10623 Berlin, Germany*
*[2] Albert-Ludwigs-Universität Freiburg, Institut für Anorganische und Analytische Chemie, Albertstr. 21, 79104 Freiburg, Germany*
*[3] Technische Universität Dresden, Fachrichtung Chemie und Lebensmittelchemie, Helmholtzstr. 10, 01069 Dresden, Germany*
*[4] Humboldt Universität zu Berlin, Institut für Chemie, Brook-Taylor-Strasse 2, 12489 Berlin, Germany*
*[5] Department of Chemistry, University College London, 20 Gordon Street, London, WC1H 0AJ, United Kingdom*
*[6] Department of Chemistry, University of Cambridge, Lensfield Road, CB2 1EW, Cambridge, United Kingdom*

* Correspondence to: ingo.zebger@tu-berlin.de, anna.fischer@ac.uni-freiburg.de

# Materials & experimental

The following chemicals were used: tetrabutylammonium tetrafluoroborate ($TBAPF_6$) (Sigma-Aldrich, Germany), tetrabutylammonium perchlorate ($TBAClO_4$) (Sigma Aldrich, Germany), acetonitrile (Extradry AcroSeal, ACROS Organics, Germany). 4-(1H-Imidazol-1-yl)aniline underwent diazotization using $NOBF_4$ to give the stable orange-brown 4-(1H-imidazol-1-yl)benzenediazonium tetrafluoroborate salt (hereby denoted $Im\text{-}N_2^+$). The method used was adapted from literature methods for the synthesis of other diazonium salts.[1,2] ESI-MS (m/z): 171.07 [$Im\text{-}N_2^+$], 143.06 [$Im^+$]. $^1H$ NMR (700 MHz, DMSO-d6, $\delta$/ppm): 8.81 (d, J = 14.7 Hz, 2H, N≡N-CC*H*), 8.73 (s, 1H, NC*H*N), 8.32 (d, J = 14.7 Hz, 2H, N≡N-CCHC*H*), 8.09 (7.32 (s, 1H, Ar-NC*H*CH), 7.32 (s, 1H, Ar-NCHC*H*).

Crystalline 8% Sb-doped $SnO_2$ (ATO) nanoparticles, where Sb% = Sb/(Sb+Sn), were synthesised *via* a non-hydrothermal synthesis route by dissolving 6.25 mmol of tin tetrachloride ($SnCl_4$ Sigma Aldrich) and 0.55 mmol on antimony acetate (Sigma Aldrich) in 5 mL toluene in a glovebox under argon atmosphere. The glass inlet with the resulting solution was transferred into an autoclave Teflon liner, capped, and then removed from the glovebox. Using a schlenk line, 15 mL of benzyl alcohol was extracted under argon and quickly added to the solution by slightly tipping the Teflon cap. The setup was then transferred into an autoclave reactor, sealed, and heated at 150 °C for 3 hrs. The glass container with the resulting clear solution was removed from the glovebox and transferred into a Teflon-lined autoclave, sealed and heated at 150 °C for 3 hrs. The resulting brown particles were removed and sequentially cleaned using 15 min of ultrasonication twice in toluene and three times in acetone. Centrifugation was used for 20 min at 5,000 rpm to separate the supernatant from the particles.

Colloidally stable solutions of ATO nanoparticles were formed by sonicating and stirring 160 mg ATO nanoparticles and 80 mg Pluronic F127 (Sigma Aldrich) in 2 mL THF with a few microliters of conc. HCl added to aid the dispersion. Mesoporous ATO (me-ATO) films were electrogred on planar ITO-coated glass substrates (pl-ITO, 8-12 Ω/sq, Sigma-Aldrich) by evaporation induced self-assembly (EISA) whereby the substrates were immersed into the solutions using a dip-coater with a 200 mm/min withdrawal rate in a 50% relative humidity at 20 °C. The resulting films were aged for 12 hrs in air at 100 °C and calcined at 450 °C for 30 min with a temperature ramp rate of 0.6 °C/min. The resulting transparent films were characterised using scanning electron microscopy (SEM). pl-ITO were cleaned sequentially by sonication for 5 min in water, ethanol and acetone before coating with me-ATO or uncoated before electrochemical measurements.

me-ATO films for attenuated total reflectance Infrared spectroscopy (ATR-IR) experiments were deposited on an un-doped Si prism (L × W × H = 25 mm × 20 mm × 9 mm) by spin-coating, followed by the same ageing and calcination steps as for the coated-ITO substrates. Spin-coating results in a continuous, even coverage of me-ATO on the prism surface with an open porous film structure, as can be seen in the photograph and SEM images in Fig. S5.

Electrochemical measurements were performed using a three-electrode set-up in which me-ATO or pl-ITO films were used as working electrodes, a Pt wire as a counter electrode and an adequate reference electrode. In aqueous solvents an Ag/AgCl 3 M KCl (Dri-Ref, WPI) reference electrode was used, while in acetonitrile a Ag/AgCl 3 M KCl (Leak-Free, Warner Instruments) reference electrode was used. Unless stated otherwise, a 0.1 M $TBAClO_4$ was used as a supporting electrolyte for measurements in acetonitrile. The potentials measured relative to the Ag/AgCl reference were converted to the reversible hydrogen electrode (RHE) scale using the Nernst equation:

$$E_{\mathrm{RHE}} = E_{\mathrm{Ag/AgCl}} + 0.059\ \mathrm{pH} + E^{\circ}_{\mathrm{Ag/AgCl}}$$

Potentials in acetonitrile were measured relative to the ferrocene/ferrocenium ($Fc/Fc^+$) couple of a 0.1 or 1 mM ferrocene solution (0.1 M $TBAClO_4$). Control of the working electrode was performed either using a CHI potentiostat or a Metrohm µAutolab potentiostat.

Imidazole-functionalised interfaces were electrochemically grafted on to me-ATO from 1 mM Im-$N_2^+$ solutions in acetonitrile (0.1 M $TBAClO_4$) by using chronoamperometry and applying a potential of -0.42 V (vs Fc/$Fc^+$) for 120 s, followed by rinsing the electrode in copious amounts of acetonitrile and dichloromethane. FePOMe was immobilised on me-ATO using two different strategies: (a) a two-step 'post-coordination' process whereby imidazole-functionalised interfaces were first electrografted from 1 mM Im-$N_2^+$ using the aforementioned method, followed by incubation with 1.2 mM FePOMe; and (b) a one-step process whereby an interface is electrochemically grafted on me-ATO directly from 1 mM Im-$N_2^+$ and 1.2 mM FePOMe (after mixing them for 5 min i.e. pre-coordinating the iron centre to the axial ligand). In each case a potential of -0.42 V (vs Fc/Fc+) is applied for 120 s, followed by copious rinsing with acetonitrile and dichloromethane. In the case of pl-ITO, to avoid the formation of thick, insulating interfaces, imidazole-functionalised interfaces were electrografted from 1 mM Im-diazo using a scanned potential in the form of a single linear sweep voltammogram (LSV) from 0.04 V to -0.86 V (vs Fc/$Fc^+$) at 50 $mVs^{-1}$, followed by incubation with FePOMe.

The surface coverages of FePOMe $\Gamma_{\mathrm{UV}}$ were determined using background subtracted absorbance values $A$ from UV-Vis absorption spectra and the following equation:

$$\Gamma_{\mathrm{UV}} = \frac{A(\lambda)}{1000 \times \varepsilon(\lambda)}$$

where $\varepsilon$ at 316 nm for FePOMe = 13600 $M^{-1}cm^{-1}$.

Surface coverages of electroactive FePOMe $\Gamma_{\mathrm{CV}}$ were determined using the following equation:

$$\Gamma_{\mathrm{UV}} = \frac{Q}{nFA}$$

where $Q$ is the integrated area of the background subtracted $Fe^{2+}/Fe^{3+}$ reduction peak, $n$ is the number of electrons passed (= 1), $F$ is the Faraday constant, and A is the surface area of the electrode. The geometric surface area of the electrode was used (0.4 $cm^2$).

The inherent electrochemical stability window of the me-ATO electrodes in pH 7 0.1 M phosphate buffer (PB) was measured as shown in Fig. S6 using a methodology developed by Jaramillo and co-workers.[3] Briefly, CVs were applied from a starting potential of -0.35 V vs RHE with progressive scans increasing by increments of 0.1 V in both cathodic and anodic directions. Scan rate = 25 $mVs^{-1}$.

X-ray photoelectron spectroscopy (XPS) was carried out using a Thermo Scientific K-Alpha instrument with monochromatic Al-Kα radiation at 1486.6 eV on an area of 400 $\mu m^2$. All spectra were charge corrected relative to the C-C component of the C 1s fitted spectra (285 eV). Survey scans were recorded with a resolution of 3 eV, while high resolution scans of the individual elements were recorded with a resolution of 5 eV. All spectra were charge corrected relative to the C-C component of the C 1s fitted spectra (285 eV). Spectra were fitted using the CasaXPS software (2.3.16) with mixed 30%/70% Gaussian/Lorentzian profiles and a Shirley background. N 1s spectra were fitted without any constraints. O 1s spectrum of the unmodified me-ATO were fitted using a Sb $3d_{5/2}$ spin-orbit component with a constrained area and peak position (9.39 eV separation from the Sb $3d_{3/2}$ component). The modified me-ATO O 1s spectrum was fitted using the same Sb $3d_{3/2}/_{5/2}$ spin-orbit separation and the ratio between the bulk lattice oxygen component and the Sb $3d_{5/2}$ was constrained to the same ratio determined for the unmodified me-ATO.

*In situ* IR measurements were performed using a Kretschmann ATR-type configuration with a me-ATO coated Si prism. Spectra were recorded from 4000 to 1000 $cm^{-1}$ with a spectral resolution of 4 $cm^{-1}$ on a Bruker IFS66v/s spectrometer equipped with a liquid nitrogen cooled photoconductive Mercury Cadmium Telluride (MCT) detector. A temperature-controlled, homemade spectroelectrochemical cell was used, maintained at a temperature of 25 $^oC$. 400 scans were averaged per IR spectrum whereby spectra were allowed to stabilise before a final spectrum was recorded. A PTFE-coated O-ring was used to seal the electrochemical cell on top of the coated prism, forming a working electrode with a geometric area of ca. 0.79 $cm^2$. Electrochemical grafting and desorption measurements were performed using 0.1 M solutions of $TBAClO_4$ in acetonitrile. $TBAPF_6$ was used for the IR spectrum in Figure 2 to avoid absorbance due to the perchlorate anion at low wavenumbers. All electrochemical measurements, unless stated otherwise, were performed under inert argon atmosphere. Following all modification steps, electrodes were thoroughly rinsed in acetonitrile and dichloromethane. All desorption measurement spectra were recorded under a constant potential of 0.79 V (vs RHE) to minimise charge-induced effects in the spectra. Individual cathodic or anodic desorption potential steps were held for 2 min.

To assign the measured ATR-IR spectra on Im-interfaces on me-ATO, DFT calculations were performed in vacuum. A phenyl-imidazole species bound to an $Sn(OH)_3$ cluster *via* a Sn-O-C bond was used to account for structural changes upon binding to the ATO surface. Geometry optimisation and vibrational analysis were performed using the BP86 level of theory through Gaussian 09.[4–6] For C, H, N, and O atoms the 6-31g* basis set was employed, while for Sn the LanL2DZ (using a pseudo core potential) was employed.[7–9] Geometry optimisations were performed using the keywords “opt=tight” and “int=ultrafine” before calculating the vibrational frequencies.

UV-vis spectroelectrochemical measurements were performed in a (Agilent) spectrometer using a custom-made set-up in a 3,500 uL quartz cuvette filled with 0.1 M phosphate buffer (PB) at pH 7.

Resonance Raman measurements of the FePOMe species were performed using a confocal Raman spectrometer (LabRam HR-800, Jobin Yvon) equipped with a liquid $N_2$ cooled CCD Symphony detector. The samples were excited using the 413 nm line of the Kr ion continuous wave laser and the laser beam was focussed on the sample using a 20× Olympus objective. The scattered light was collected in a 180° back-scattering geometry. The laser power was adjusted for each experiment, with a final laser power of between 1-2 MW. Spectra were calibrated against the Raman shift of Hg, which is positioned at 435.834 nm. Spectra were collected with a spectral resolution of 1-2 $cm^{-1}$. Spectroelectrochemical measurements were performed using the home-made PTFE cell mentioned previously with a three-electrode configuration. The cell consisted of a Ag/AgCl 3M KCl (Leak-Free, Warner Instruments) reference electrode, a platinum wire counter electrode a me-ATO film on ITO-coated glass as a working electrode. The cell was rotated by means of a rotating table to avoid photoinduced processes, such as photodegradation or photoreduction. Measurements were performed at room temperature. Spectra were evaluated using the home-made qpipsi software, with component fit analysis used to assign porphyrin vibrational modes. Peaks were fitted with Lorentzian curves.

# Figures

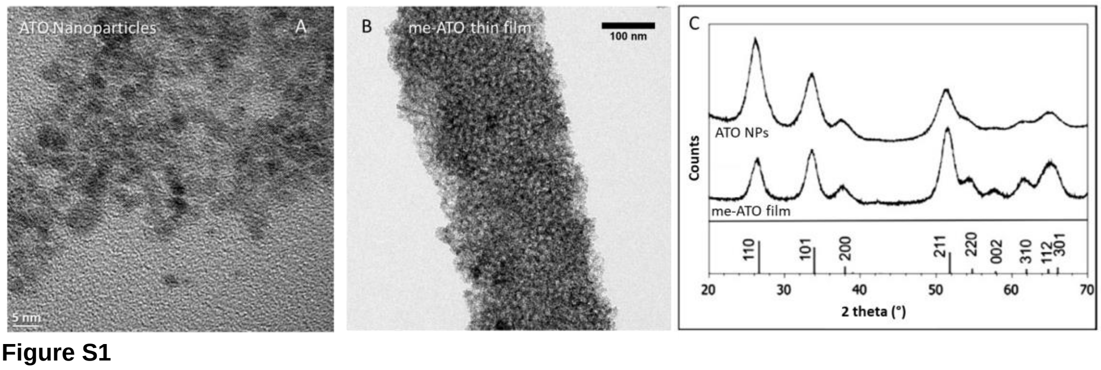

**Figure S1**
(a) High-resolution TEM images of the synthesised ATO nanoparticles, (b) TEM images of a piece of a mesoporous ATO film scratched from the surface and (c) XRD pattern of the ATO nanoparticles used to build the me-ATO films and of the me-ATO films after calcination.

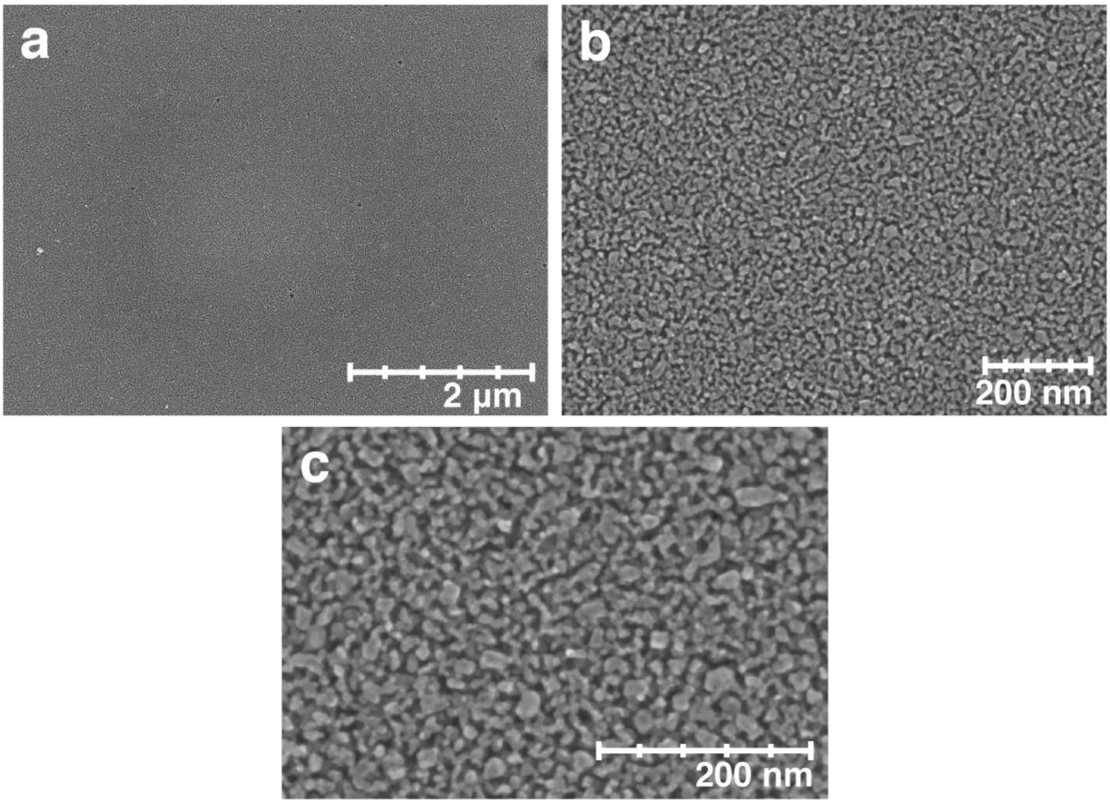

**Figure S2**
(a-c) Top view SEM images of the me-ATO films at increasing magnifications.

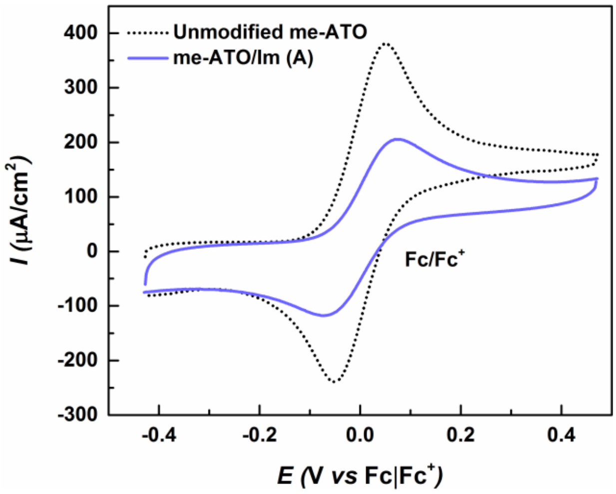

**Figure S3**
CVs of 1 mM ferrocene in acetonitrile (0.1 M $TBAClO_4$) of me-ATO before and after electrografting with $Im\text{-}N_2^+$ for 120 s at a potential of -0.42 V (vs $Fc/Fc^+$).

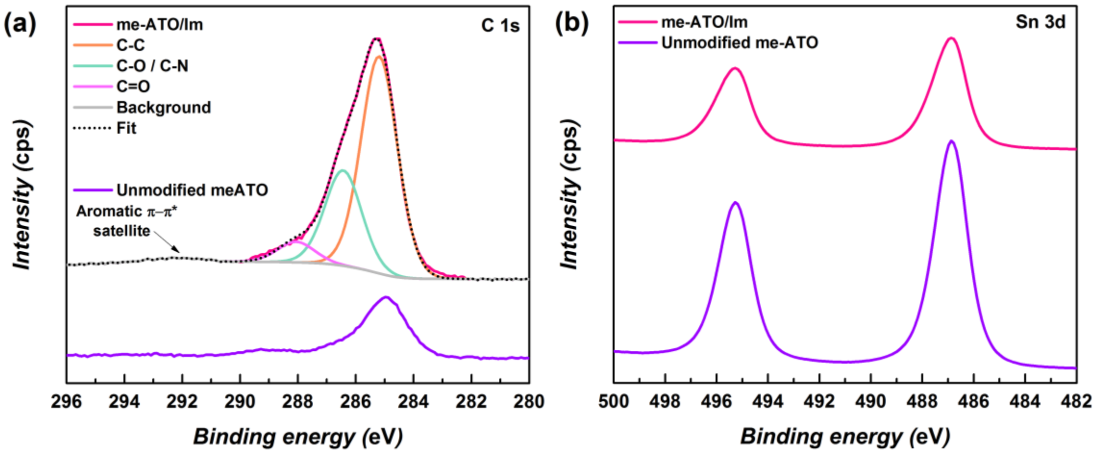

**Figure S4**
The deconvoluted C 1s (left) and Sn 3d (right) XP spectra of me-ATO before and after electrografting with Im-$N_2^+$.

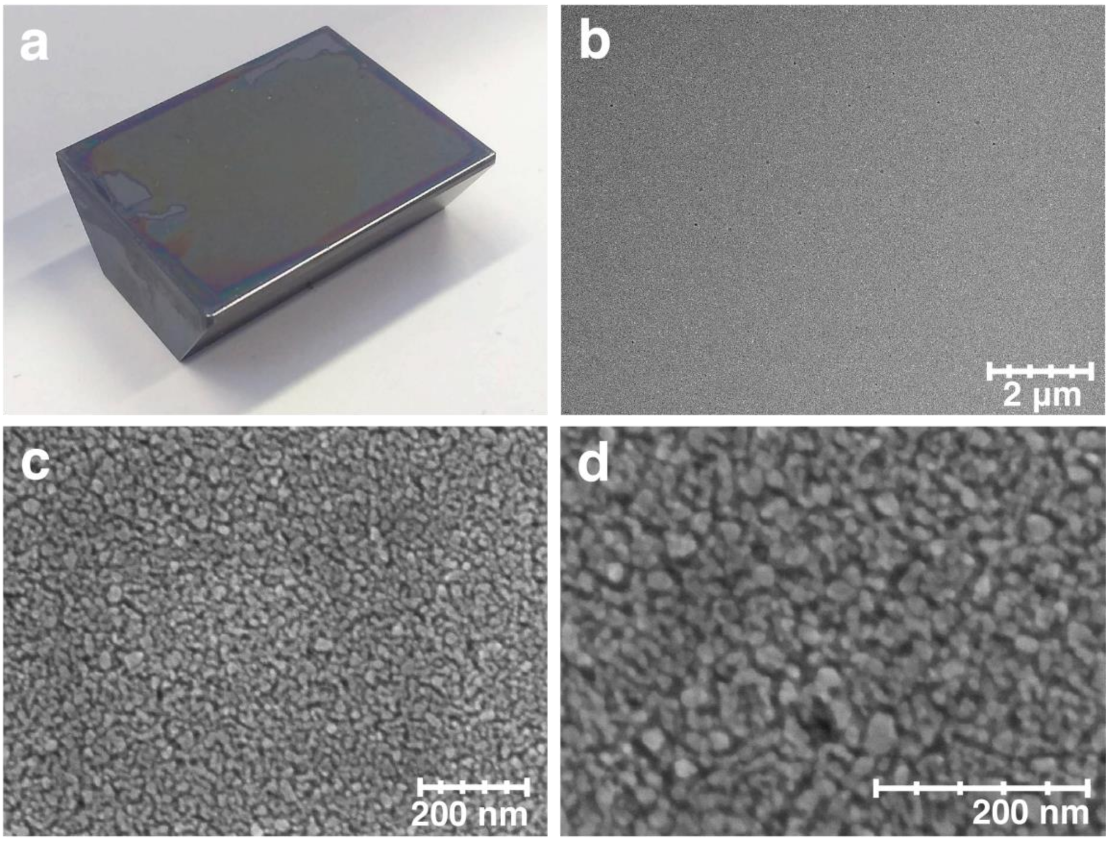

**Figure S5**
(a) Photograph of me-ATO film spin-coated on a Si prism and (b-d) top view SEM images of the film at increasing magnifications.

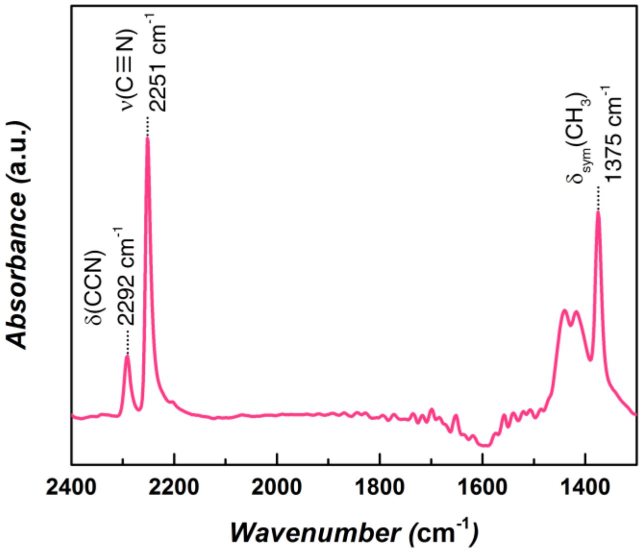

**Figure S6**
IR spectrum in ATR mode of me-ATO in acetonitrile.

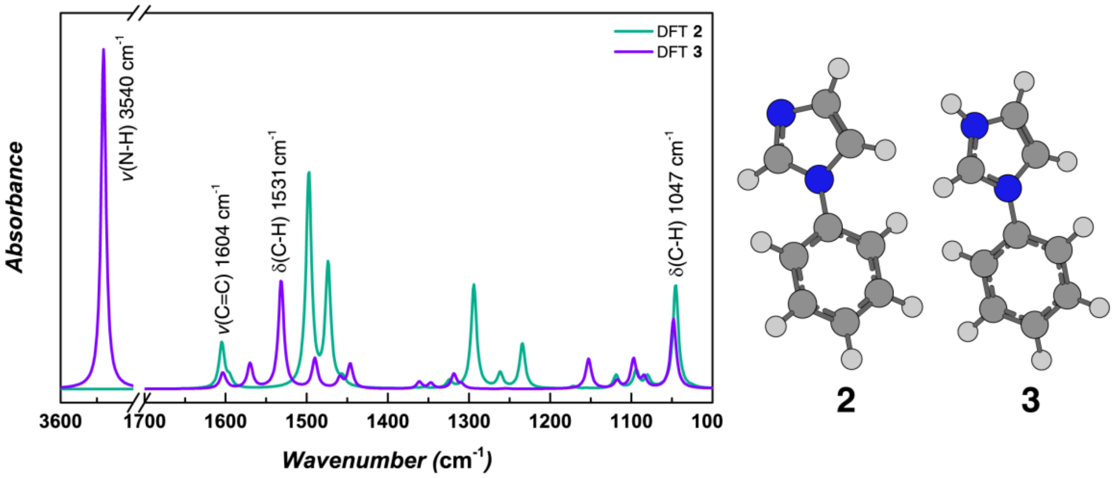

**Figure S7**
IR spectra calculated using DFT of 1-phenyl-1H-imidazole **2** and its protonated imidazolium analogue **3**. Right: optimised structures of **2** and **3**, atom labels: carbon (dark grey), hydrogen (light grey), nitrogen (blue).

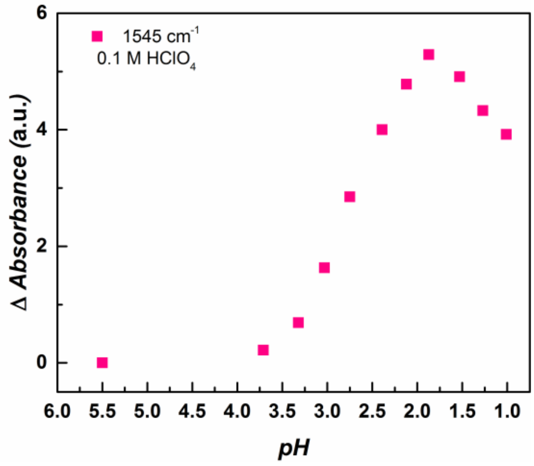

**Figure S8**
Plot of change in absorption intensity ΔA with decreasing pH for the C-H bending mode δ(C-H) at 1545 cm$^{-1}$.

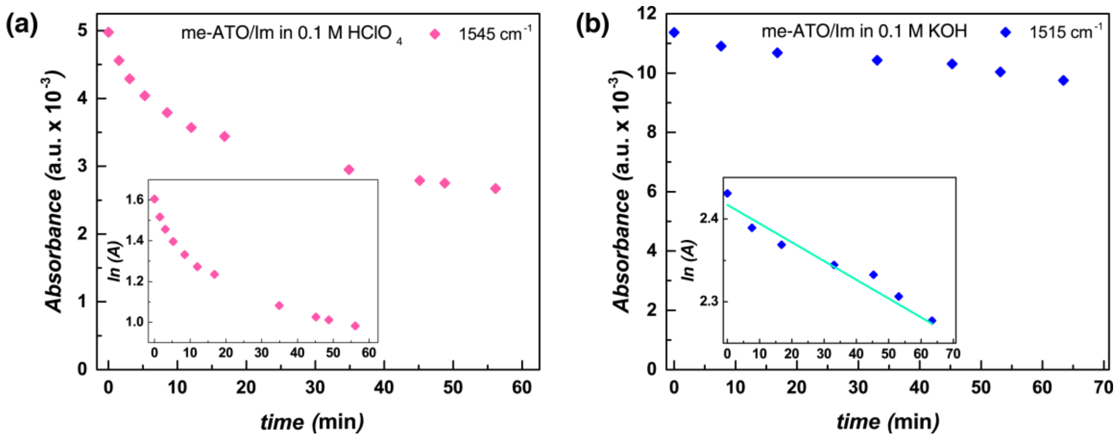

**Figure S9**

Plots of δ(C-H) IR band intensities versus time for the electrografted diazonium interfaces on me-ATO in (a) 0.1 M $HClO_4$ and (b) 0.1 M KOH. The wavenumber of the bands used are indicated in the legend. Plots of the natural logarithm (ln) of the absorbance versus time are shown in the insets.

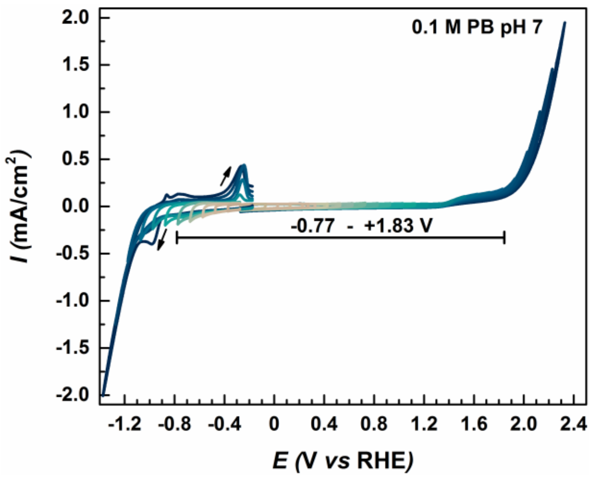

**Figure S10**

CVs conducted in 0.1 M PB pH 7 using me-ATO as a working electrode in order to determine the stability range of the electrode. Progressive scans with increments of 0.1 V were applied in both cathodic and anodic directions originating from a potential of -0.35 V (vs RHE). Scan rate = 25 mVs$^{-1}$.

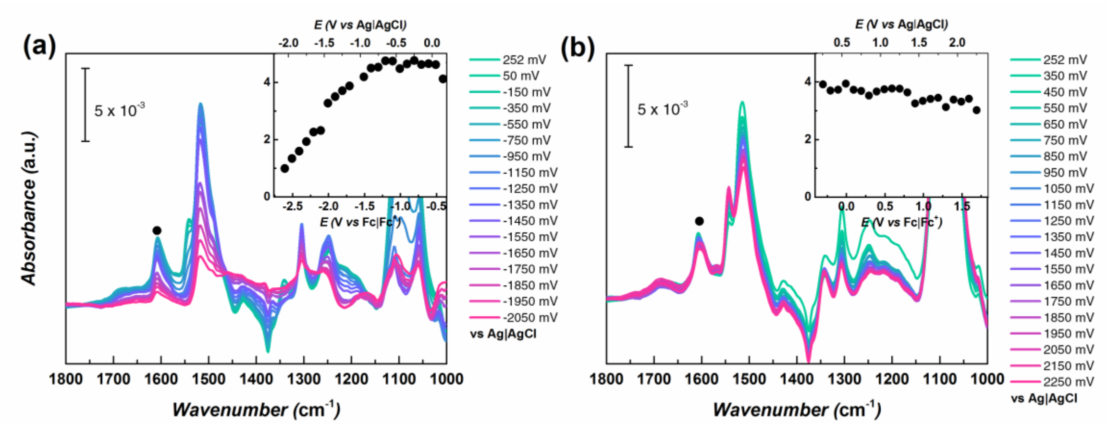

**Figure S11**

*In situ* IR spectra in ATR mode of Im-interfaces electrografted on me-ATO in acetonitrile (0.1 M $TBAClO_4$) after 2-minute-long applications of increasingly (a) cathodic or (b) anodic potential steps. Insets: plots of the corresponding $v(C=C)_{ar}$ band intensities at 1608 cm$^{-1}$ versus applied potential.

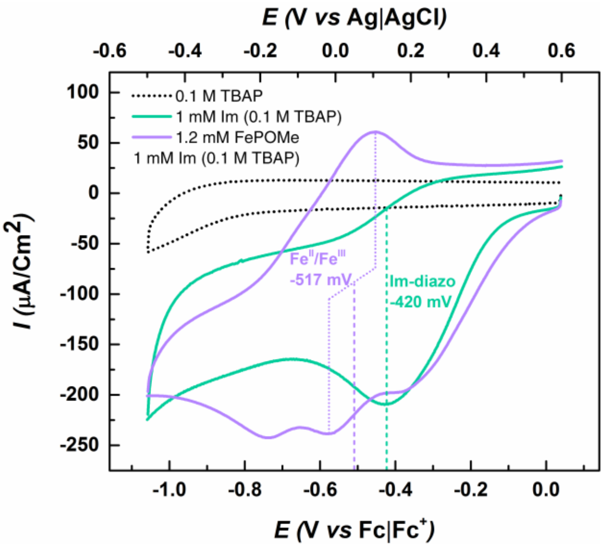

**Figure S12**

CVs of 1 mM solutions of $Im\text{-}N_2^+$ in acetonitrile (0.1 M $TBAClO_4$) using me-ATO as a working electrode, with and without addition of 1.2 mM FePOMe. Scan rate = 50 $mVs^{-1}$.

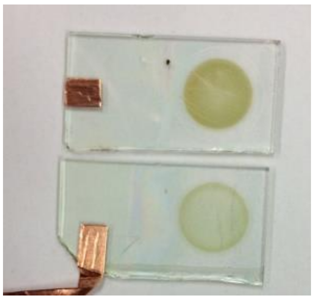

**Figure S13**

Photograph of me-ATO coated pl-ITO electrodes immobilised with FePOMe using (top) the 'pre-coordination' or (bottom) 'post-coordination' methods.

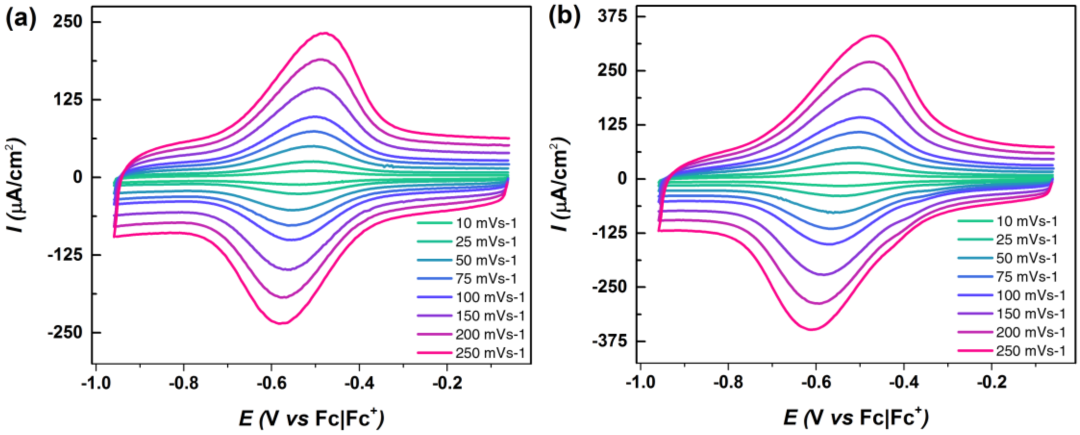

**Figure S14**

CVs in acetonitrile (0.1 M $TBAClO_4$) of FePOMe immobilised on me-ATO modified using (a) the 'post-coordination' and (b) 'pre-coordination' methods at different scan rates.

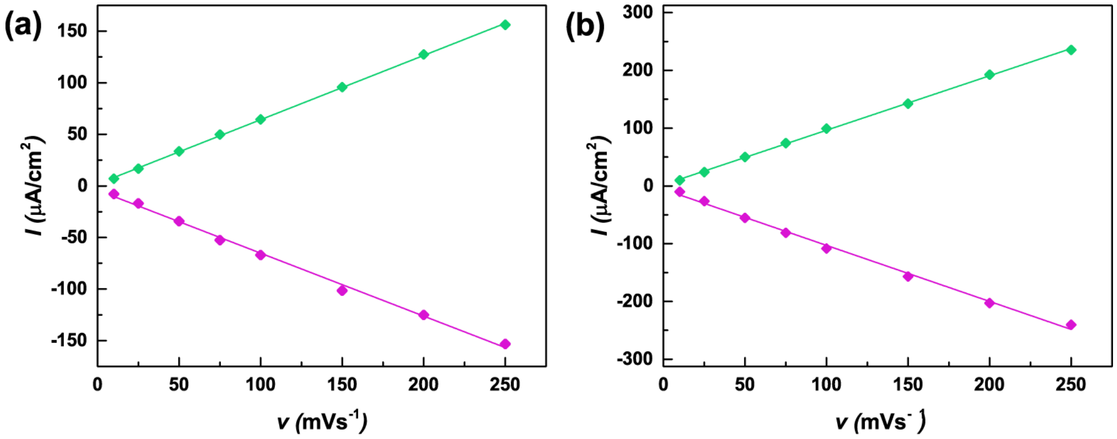

**Figure S15**
Plot of peak currents $I_p$ vs scan rates $v$ for FePOMe immobilised on me-ATO via (a) the 'post-coordination' and (b) 'pre-coordination' methods.

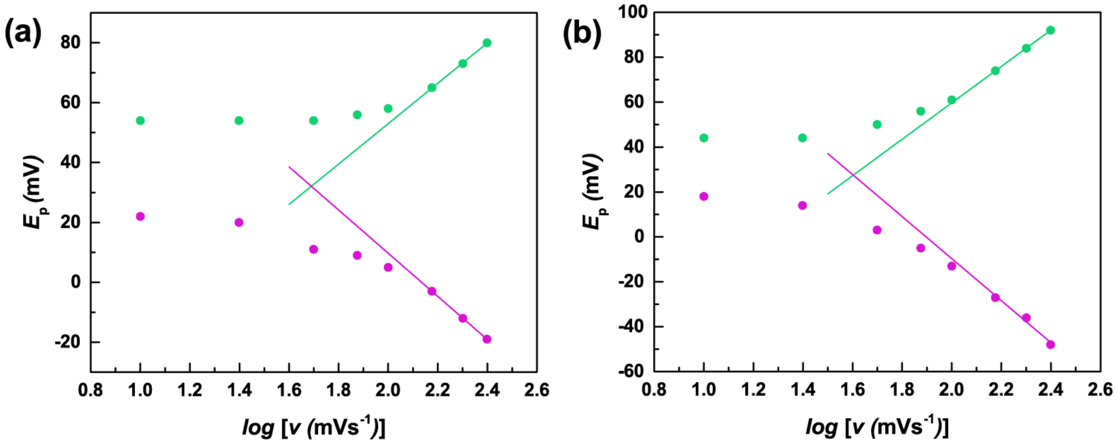

**Figure S16**
Plots of peak separation $\Delta E_p$ vs the log of the scan rate log($v$) for the $Fe^{2+}/Fe^{3+}$ redox couple of FePOMe immobilised on me-ATO modified *via* the (a) 'post-coordination' and (b) 'pre-coordination' methods.

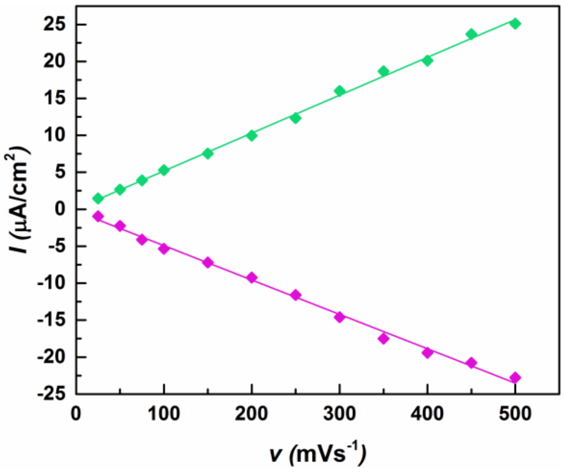

**Figure S17**
A plot of peak currents $I_p$ vs scan rates $v$ for FePOMe immobilised on pl-ITO using the 'post-coordination' method.

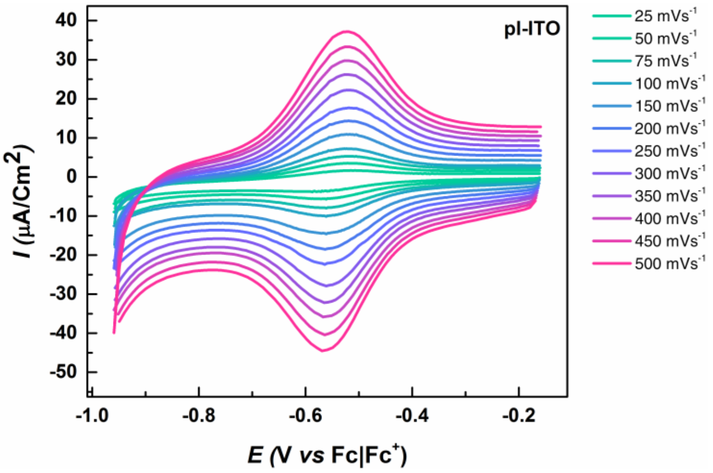

**Figure S18**

CVs in acetonitrile (0.1 M $TBAClO_4$) of FePOMe immobilised on pl-ITO using the 'post-coordination' method. Note: the peak separation remains constant at each scan rate.

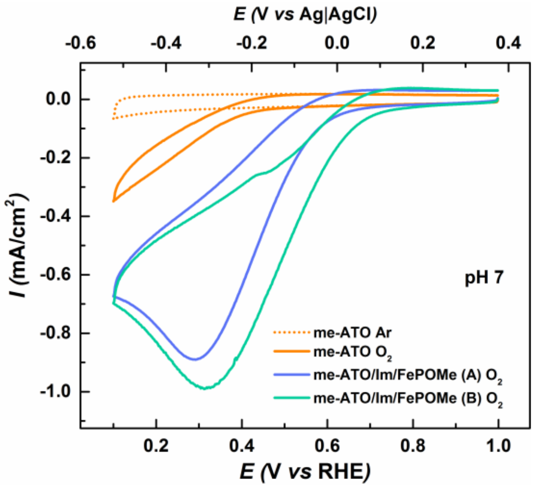

**Figure S19**

CVs of unmodified me-ATO in pH 7 (0.1 M PB) under Ar and $O_2$ bubbling, as well as me-ATO with FePOMe immobilised using the 'post-coordination' (labelled A, blue trace) and 'pre-coordination' (labelled B, green trace) methods.

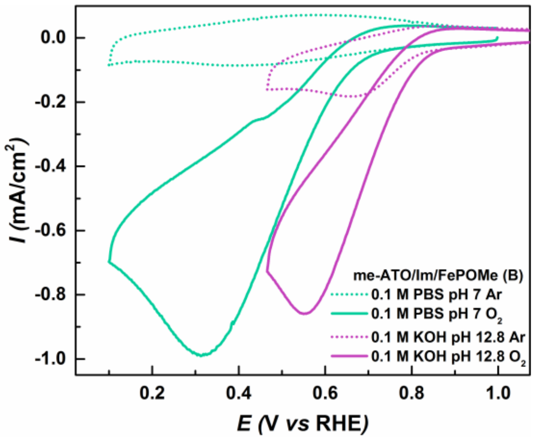

**Figure S20**

CVs of me-ATO in pH 7 (0.1 M PB) and pH 12.8 (0.1 M KOH) under $O_2$ or Ar bubbling with FePOMe immobilised using the 'pre-coordination' method.

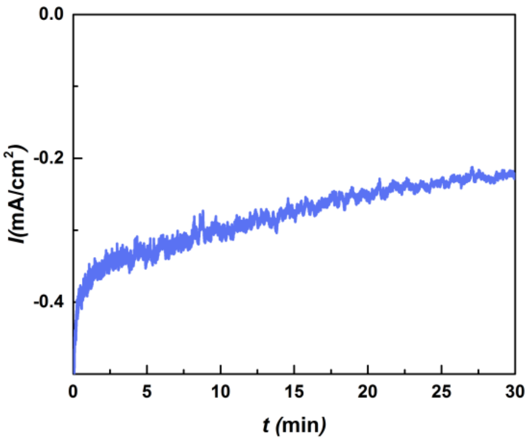

**Figure S21**
Chronoamperometric measurements at 0.32 V (vs RHE) under $O_2$ bubbling extended for a further 30 min for the FePOMe immobilised on me-ATO using 'post-coordination' method.

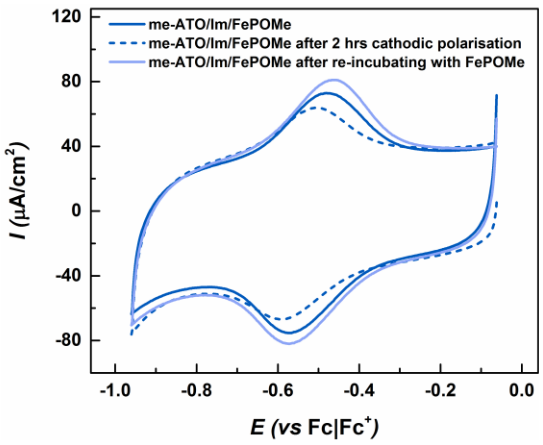

**Figure S22**
CVs in acetonitrile (0.1 M $TBAClO_4$) of FePOMe immobilised on me-ATO using 'post-coordination' before and after cathodic polarisation in pH 7 (0.1 M PB) in air for ca. 2 hrs in pH 7, and then again after re-incubating with fresh FePOMe.

# Tables

**Table S1** Binding energies (in eV) of the individual deconvoluted components of the XPS N 1s and O 1s spectra recorded for unmodified me-ATO and the me-ATO electrografted with $Im\text{-}N_2^+$.

| | ***Binding energy (eV)*** | |
|---|---|---|
| | N 1s | O 1s |
| *me-ATO* | | 530.8 |
| | | 532.0 |
| *me-ATO/Im* | 399.2 | 530.9 |
| | 400.1 | 531.9 |
| | 401.1 | |
| | 402.1 | |

**Table S2**
A comparison between surface coverages $\Gamma_{CV}$ of molecular catalysts and redox species on different porous oxide electrodes of different film thicknesses from the literature.

| ***Redox species*** | ***Electrode*** | ***Film thickness ($\mu$M)*** | ***Coverage (× $10^{-9}$ molcm$^{-2}$)*** | ***Volume coverage (× $10^{-5}$ molcm$^{-3}$)*** | ***Ref.*** |
|---|---|---|---|---|---|
| *[Ru(bpy)$_2$(4,40-PO$_3$H$_2$-bpy)](PF$_6$)$_2$ - Phosphonate* | Porous ITO | 0.55<br>2.5<br>15.7 | 5.5<br>25<br>160<br>(UV-Vis) | ~ 10 | [10] |
| *[Co$^{III}$Br$_2${(DO)(DOH)pn}] - Phosphonate* | Porous ITO | 13 | ~ 150<br>(UV-Vis) | ~12 | [11] |
| *Various Co catalysts - Phosphonate* | Porous ITO | 13 | 22 – 28<br>(CV) | ~ 2 | [12] |
| *[Ru(Mebimpy)(4,4'-((HO)$_2$-OPCH$_2$)$_2$bpy)(OH$_2$)]$_2^+$ - - Phosphonate* | Porous TiO$_2$ | ~ 10 | 53<br>(UV-Vis) | ~ 5.3 | [13] |
| *Ni$^{II}$ bis(diphosphine) complex - Phosphonate* | Porous TiO$_2$ | 4 | 146<br>(UV-Vis) | ~ 37 | [14] |
| *fac-[MnBr(4,4'-bis(PO$_3$H$_2$)-2,2'-bipyridine)(CO)$_3$] - Phosphonate* | Porous TiO$_2$ | 6 | 34<br>(UV-Vis) | ~ 6 | [15] |
| *[Ru$^{II}$(Mebimpy)(4,4'-(PO$_3$H$_2$)$_2$bpy) (OH$_2$)]$^{2+}$ - Phosphonate* | Mesoporous ATO | 2 | 248<br>(UV-Vis)<br>1.58<br>(CV) | ~ 12<br>~ 8 | [16] |
| *Ferrocene carboxylic acid (via amide-coupling to 3-aminopropyltrietoxysilane - Silane* | Mesoporous ATO | 0.21 | 0.9 – 0.6<br>(CV) | ~ 3 | [17] |
| *FePOMe ('post-coordination') - Diazonium* | Mesoporous ATO | 0.16 | 1.5<br>(UV-Vis)<br>1.5<br>(CV) | ~ 9.4<br>~ 9.4 | This work |
| *FePOMe ('pre-coordination') - Diazonium* | Mesoporous ATO | 0.16 | 3.9<br>(UV-Vis)<br>3.0<br>(CV) | ~ 24<br>~ 19 | This work |

**Table S3**
A comparison of the redox potentials $E_0$ and electron transfer rates ($k_{ET}$) for the Fe($^{2+/3+}$) redox couple of the system presented here and different molecular/enzymatic redox species from literature immobilised on different porous oxide electrodes of different film thicknesses. Potentials are given versus RHE and were calculated using the Nernst equation.

| ***Redox species*** | ***Electrode*** | ***Film thickness ($\mu$M)*** | ***$E^{\circ}$(Fe$^{2+/3+}$) (V vs RHE)*** | ***$k_{ET}$ (s$^{-1}$)*** | ***Ref.*** |
|---|---|---|---|---|---|
| *Cytochrome C* | Mesoporous ITO | 0.17 | 0.425 | 1.2 | [18] |
| *Cytochrome C* | Mesoporous ITO | 2 | 0.670 | 12 | [19] |
| *Fe mimochrome* | Mesoporous ITO | 1 | 0.274 | 4 | [20] |
| *Microperoxidase-11* | Mesoporous ITO | 0.2 | 0.263 | 10 | [21] |
| *Cytochrome C* | Mesoporous SnO$_2$ | 4 | 0.673 | 1 | [22] |
| *Fe tetra(2,6-dihydroxyphenyl) porphyrin* | Carbon nanotubes | - | 0.330 | - | [23] |
| *Microperoxidase-11* | Mesoporous ATO | 0.42 | 0.274 | 1.5 | [24] |
| *FePOMe (A)* | Mesoporous ATO | 0.16 | 0.429 | 4.4 | This work |

| | | | | | |
|---|---|---|---|---|---|
| *FePOMe (B)* | Mesoporous ATO | 0.16 | 0.496 | 4.9 | This work |

## References

1 A. Mesnage, X. Lefèvre, P. Jégou, G. Deniau and S. Palacin, *Langmuir*, 2012, **28**, 11767–78.
2 D. V Kosynkin and J. M. Tour, *Org. Lett.*, 2001, **3**, 993–995.
3 J. D. Benck, B. A. Pinaud, Y. Gorlin and T. F. Jaramillo, *PLoS One*, 2014, **9**, e107942.
4 A. D. Becke, *Phys. Rev. A*, 1988, **38**, 3098–3100.
5 J. P. Perdew, *Phys. Rev. B*, 1986, **33**, 8822–8824.
6 M. J. Frisch, G. W. Trucks, H. B. Schlegel, G. E. Scuseria, M. A. Robb, J. R. Cheeseman, G. Scalmani, V. Barone, B. Mennucci, G. A. Petersson, H. Nakatsuji, M. Caricato, X. Li, H. P. Hratchian, A. F. Izmaylov, J. Bloino, G. Zheng, J. L. Sonnenberg, M. Hada, M. Ehara, K. Toyota, R. Fukuda, J. Hasegawa, M. Ishida, T. Nakajima, Y. Honda, O. Kitao, H. Nakai, T. Vreven, J. Montgomery, J. A., J. E. Peralta, F. Ogliaro, M. Bearpark, J. J. Heyd, E. Brothers, K. N. Kudin, V. N. Staroverov, R. Kobayashi, J. Normand, K. Raghavachari, A. Rendell, J. C. Burant, S. S. Iyengar, J. Tomasi, M. Cossi, N. Rega, J. M. Millam, M. Klene, J. E. Knox, J. B. Cross, V. Bakken, C. Adamo, J. Jaramillo, R. Gomperts, R. E. Stratmann, O. Yazyev, A. J. Austin, R. Cammi, C. Pomelli, J. W. Ochterski, R. L. Martin, K. Morokuma, V. G. Zakrzewski, G. A. Voth, P. Salvador, J. J. Dannenberg, S. Dapprich, A. D. Daniels, Ö. Farkas, J. B. Foresman, J. V. Ortiz, J. Cioslowski and D. J. Fox, *Gaussian 09, Revision D.01*, Gaussian, Inc., Wallingford CT, 2013.
7 F. Weigend and R. Ahlrichs, *Phys. Chem. Chem. Phys.*, 2005, **7**, 3297–3305.
8 Y. Rippers, T. Utesch, P. Hildebrandt, I. Zebger and M. A. Mroginski, *Phys. Chem. Chem. Phys.*, 2011, **13**, 16146–16149.
9 J. Kozuch, C. Weichbrodt, D. Millo, K. Giller, S. Becker, P. Hildebrandt and C. Steinem, *Phys. Chem. Chem. Phys.*, 2014, **16**, 9546–9555.
10 P. G. Hoertz, Z. Chen, C. A. Kent and T. J. Meyer, *Inorg. Chem.*, 2010, **49**, 8179–8181.
11 N. M. Muresan, J. Willkomm, D. Mersch, Y. Vaynzof and E. Reisner, *Angew. Chemie - Int. Ed.*, 2012, **51**, 12749–12753.
12 J. Willkomm, N. M. Muresan and E. Reisner, *Chem. Sci.*, 2015, **6**, 2727–2736.
13 Z. Chen, J. J. Concepcion, J. W. Jurss and T. J. Meyer, *J. Am. Chem. Soc.*, 2009, **131**, 15580–15581.
14 T. E. Rosser, M. A. Gross, Y.-H. Lai and E. Reisner, *Chem. Sci.*, 2016, **7**, 4024–4035.
15 T. E. Rosser, C. D. Windle and E. Reisner, *Angew. Chem. Int. Ed. Engl.*, 2016, **55**, 7388–7392.
16 H. Luo, Z. Fang, N. Song, T. Garvey, R. Lopez and T. J. Meyer, *ACS Appl. Mater. Interfaces*, 2015, **7**, 25121–25128.
17 V. Müller, M. Rasp, J. Rathouský, B. Schütz, M. Niederberger and D. Fattakhova-Rohlfing, *Small*, 2010, **6**, 633–7.
18 S. Frasca, T. von Graberg, J. J. Feng, A. Thomas, B. M. Smarsly, I. M. Weidinger, F. W. Scheller, P. Hildebrandt and U. Wollenberger, *ChemCatChem*, 2010, **2**, 839–845.
19 D. Schaming, C. Renault, R. T. Tucker, S. Lau-Truong, J. Aubard, M. J. Brett, V. Balland and B. Limoges, *Langmuir*, 2012, **28**, 14065–14072.
20 R. Vitale, L. Lista, S. Lau-Truong, R. T. Tucker, M. J. Brett, B. Limoges, V. Pavone, A. Lombardi and V. Balland, *Chem. Commun.*, 2014, **50**, 1894–1896.
21 C. Renault, K. D. Harris, M. J. Brett, V. Balland and B. Limoges, *Chem. Commun.*, 2011, **47**, 1863–1865.
22 E. Topoglidis, Y. Astuti, F. Duriaux, M. Grätzel and J. R. Durrant, *Langmuir*, 2003, **19**, 6894–6900.
23 A. Maurin and M. Robert, *Chem. Commun.*, 2016, **52**, 12084–12087.
24 B. Neumann, P. Kielb, L. Rustam, A. Fischer, I. M. Weidinger and U. Wollenberger, *ChemElectroChem*, 2017, **4**, 913–919.